

# Numerical evidences for the angular momentum-mass inequality for multiple axially symmetric black holes

Sergio Dain

*Facultad de Matemática, Astronomía y Física, Universidad Nacional de Córdoba,  
Ciudad Universitaria (5000) Córdoba, Argentina; and*

*Max Planck Institute for Gravitational Physics (Albert Einstein Institute) Am Mühlenberg 1 D-14476 Potsdam Germany.*

Omar Ortiz

*Facultad de Matemática, Astronomía y Física, Universidad Nacional de Córdoba,  
Ciudad Universitaria (5000) Córdoba, Argentina.*

(Dated: November 25, 2018)

We present numerical evidences for the validity of the inequality between the total mass and the total angular momentum for multiple axially symmetric (non-stationary) black holes. We use a parabolic heat flow to solve numerically the stationary axially symmetric Einstein equations. As a by product our method, we also give numerical evidences that there are no regular solutions of Einstein equations that describe two extreme, axially symmetric black holes in equilibrium.

PACS numbers: 04.20.Dw, 04.25.dc, 04.25.dg, 04.70.Bw

## I. INTRODUCTION

The final state of a gravitational collapse is expected to be described by a black hole and not by a naked singularity. Moreover, at late times, the system should settle down to a stationary regime and since the Kerr black hole is expected to be the only stationary black hole in vacuum, the final state of all possible gravitational collapses should approach to a Kerr black hole. For simplicity, in this discussion we are not considering electromagnetic fields and also we are assuming that at some finite time all the matter fields have fallen into the black hole.

The above considerations roughly encompass what is known as the standard picture of the gravitational collapse which, in particular, includes the weak cosmic censorship conjecture. To prove that this heuristic picture is in fact a consequence of the Einstein field equations is one of the most relevant open problems in classical General Relativity.

One fruitful strategy to study some aspects of this problem is the following. From the heuristic picture presented above it is possible to deduce some geometric inequalities on the initial conditions for gravitational collapse. Hence, initial conditions that violate these inequalities would automatically provide counter examples for the validity of the standard picture of the gravitational collapse. In fact, the original intention of this strategy, proposed first by Penrose [1], was to construct such counter examples. However it was not possible to find them. It was then natural trying to prove these inequalities. Such proofs provide an indirect but highly non trivial evidence that the heuristic picture of the gravitational collapse is correct (see the discussion in [2]). This kind of inequalities are also interesting by themselves because they provide unexpected mathematical connections between geometric quantities.

A prominent example of this idea is the Penrose inequality which relates the mass with the area of the black

hole horizon on the initial conditions. An important special case of this inequality has been proved in [3] [4] (see also the review article [5]). Another example of this kind of inequalities is the inequality between mass and angular momentum. This inequality, which constitute the main subject of the present article, arises as follows.

Consider an axially symmetric gravitational collapse. An important feature of axial symmetry is that axially symmetric waves can not carry angular momentum. In other words: in vacuum, angular momentum is a conserved quantity in axial symmetry. Let us assume that the heuristic picture presented above is correct. Denote by  $m_0$  and  $J_0$  the mass and angular momentum of the final Kerr black hole. The Kerr black hole satisfies the inequality

$$\sqrt{|J_0|} \leq m_0. \quad (1)$$

The Kerr solution is well defined for any choice of the parameters  $m_0$  and  $J_0$ , it defines however a black hole only if inequality (1) is satisfied. Let  $m$  and  $J$  be the total mass and total angular momentum of the initial conditions. Since gravitational waves carry positive mass we have  $m_0 \leq m$  (this inequality is of course also valid without the assumption of axial symmetry). And because angular momentum is conserved in axial symmetry we have  $J = J_0$ . Hence, in order to reach the inequality (1) at a late time, every initial condition for axially symmetric collapse must satisfy

$$\sqrt{|J|} \leq m. \quad (2)$$

See [6] for a more detailed physical discussion. This inequality involves only quantities defined on the initial conditions. It is expected to hold for every axially symmetric vacuum (not necessarily stationary) black hole. The inequality (2) was studied in a series of articles [7] [8] [6] and finally proved for the case of one black hole in [9] and [10]. There exists however no proof for the case

of multiple axially symmetric black holes. This problem appears to be deeper (and considerable more difficult) than the single black hole case. In particular, it is related, as we discuss below, with the still open problem of the uniqueness of the Kerr black hole among stationary black holes with disconnected horizons. The main purpose of this article is to provide numerical evidence for the validity of (2) for multiple black holes.

A naive method to test (2) is to take some configuration of axially symmetric black holes and compute numerically the mass and the angular momentum of it. For a given configuration the relevant parameters are the separation distance between the black holes and the individual angular momentum of them. But, of course, these parameters (or any other finite set of parameters) do not characterize uniquely the initial conditions. There exists infinitely many configurations with the same parameters, this essentially corresponds to the freedom of including gravitational waves surrounding the black holes. Then, either we find a counter example or this naive method will give a very poor evidence in favor of (2). Just some isolated points in the space of all possible initial conditions.

Fortunately a different approach is possible. It is based on the variational principle for the inequality (2) presented in [7]. This variational principle states that the minimum of the mass of a given configuration with fixed angular momentum is achieved by the associated (i.e. with the same parameters) stationary and axially symmetric solution of Einstein equations. Hence, in order to prove the inequality (2) for a given configuration it is enough to compute the mass of the corresponding stationary and axially symmetric solution of Einstein equations, which is characterized by the separation distance and individual angular momentum of the black holes. The stationary and axially symmetric Einstein equations are non linear elliptic equations. In this article, we use a heat flow to numerically solve them. This parabolic flow has two important properties, first for arbitrary data it converges (as time goes to infinity) to a stationary and axially symmetric solutions of Einstein equations. Second, the mass is monotonically decreasing along the evolution and the angular momentum is conserved (under appropriate boundary conditions). Hence, the flow provides an accurate procedure for computing the minimum of the mass of each possible configuration. This method is interesting by itself as a method for solving numerically the stationary axially symmetric Einstein equations with prescribed boundary conditions, which, up to the best of our knowledge, have not been used so far.

For simplicity we will restrict ourselves to configurations with only two black holes, although our method applies for any number of black holes. For this configuration, the most favorable case to violate the inequality (2) is when the black holes have the same angular momentum pointing in the same direction. This corresponds to a repulsive spin-spin force between them. This is also the most favorable case for reaching a stationary solu-

tion representing two black holes at equilibrium, because it is in principle conceivable that the repulsive spin force balance the gravitational attraction. This configuration has only two parameters, the separation distance and the angular momentum. However, as we will see in the next section, due to the scale invariance of the equations we have only one non trivial parameter, which we chose to be the separation distance. We can compute the mass for every choice of the separation distance and plot a curve. From the shape of the curve it is clear that, although we can compute only a finite range, the inequality will be satisfied for every separation distance. For other configurations we proceed in similar way. Then, we obtain fairly strong numerical evidences that the inequality is satisfied for two black holes with any separation distances and any angular momentum.

As we mention above, the heat flow relaxes to a solution of the stationary and axially symmetric Einstein vacuum equations. An important open problem in General Relativity is whether the Kerr black hole is unique among stationary black holes (see the recent article [11] and reference therein). This is essentially the same problem as whether is possible to achieve an equilibrium configuration of multiple black holes in General Relativity. This problem have been studied in [12][13] [14][15][16] [17]. For some limit cases and also for cases with reflection symmetry it has been proved that equilibrium is not possible. Also, from a different perspective, the problem has been studied using exact solutions in [18]. Again, the conclusion was that equilibrium is not possible for this class of solutions. Using the heat flow, in this article we also provide numerical evidences that there is no regular equilibrium solution for two extreme black holes. This case has not been analyzed previously in the literature.

The plan of the article is the following. In section II we introduce the heat flow and analyze its main properties. We also discuss the precise form of the conjecture regarding inequality (2) and its relation with the black hole equilibrium problem mentioned above. In section III we discuss the numerical techniques used to solve the parabolic heat flow equations. In section IV we present our results and in section V we give some further perspective on the open problems. Finally, for the sake of completeness, we include an appendix A with the explicit form of the extreme Kerr solution used in our computations.

## II. THE VARIATIONAL PROBLEM AND THE PARABOLIC FLOW

Consider a vacuum, axially symmetric spacetime. The axial Killing vector defines two geometrical scalars, the square of its norm  $\eta$  and the twist potential  $\omega$ . These scalars characterize the spacetime in the following sense. Take a foliation of Cauchy surfaces on the spacetime with the corresponding time function. An initial data set for the spacetime is determined by the value of the functions

$(\eta, \omega)$  and the time derivatives  $(\eta', \omega')$  on a Cauchy surface. The Einstein evolution equations essentially reduce to a non-linear system of wave equations for  $(\eta, \omega)$ . In appropriate coordinates, the total mass  $m$  of the spacetime can be written as a positive integral on a Cauchy surface in terms of  $(\eta, \omega)$  and  $(\eta', \omega')$ . This integral is the non linear and conserved energy of the system of waves equations (see [19] for details).

An initial data set is called ‘‘momentary stationary’’ if  $(\eta', \omega')$  vanished. Stationary data are a particular class of momentary stationary data for which the scalars  $(\eta, \omega)$  satisfy a set of elliptic equations (see equations (13)–(14) below). An important feature of the mass integral is that, for arbitrary data, the associated momentary stationary data has less or equal mass. That is, there exists a lower bound for the mass that can be written in terms only on  $(\eta, \omega)$  and no time derivatives  $(\eta', \omega')$  are involved. This lower bound for the mass plays a key role in order to reduce the proof of the inequality (2) to a pure variational problem. It can be written as an integral in  $\mathbb{R}^3$  as follows (for details see [9], [20], [7], [6]).

Let  $x^i$  be Cartesian coordinates in  $\mathbb{R}^3$  (denoted also by  $x = x^1, y = x^2, z = x^3$ ) and let  $(\rho, \phi)$  be the associated cylindrical coordinates defined by  $\rho = \sqrt{x^2 + y^2}$ ,  $\tan \phi = y/x$ . The positions of the black holes will be prescribed by a finite collection of points  $i_k$  located at the  $z$  axis. More precisely, the points  $i_k$  will represent extra asymptotic ends on the spacetime and they can be associated with the location of the black holes. For a given set of  $N + 1$  points  $i_k$  we define the separation intervals  $I_k, 0 \leq k \leq N - 1$ , to be the open sets in the axis between  $i_k$  and  $i_{k-1}$ , and we define  $I_0$  and  $I_N$  as  $z < i_0$  and  $z > i_N$  respectively. Let  $L_k$  be the length of  $I_k$  for  $0 \leq k \leq N - 1$ . See figure 1. The length  $L_k$  (which are measured with respect to the Cartesian coordinates introduced above) will be associated with the separation distance between the black holes (see the discussion in [21]).

From the square norm  $\eta$  of the Killing vector we define the following function  $\sigma$

$$\eta = \rho^2 e^\sigma. \quad (3)$$

The lower bound of the mass is given by the following functional

$$\mathcal{M}(\sigma, \omega) = \frac{1}{32\pi} \int_{\mathbb{R}^3} (|\partial\sigma|^2 + \rho^{-4} e^{-2\sigma} |\partial\omega|^2) d\mu, \quad (4)$$

where  $d\mu$  is the volume element of  $\mathbb{R}^3$ ,  $\partial_i$  denotes partial derivatives with respect to Cartesian coordinates  $x^i$  and  $|\partial\sigma|^2 = \partial_i \sigma \partial^i \sigma$ . As we mentioned above, for an arbitrary axially symmetric initial data  $(\eta, \omega, \eta', \omega')$  with mass  $m$  we have that (see [9])

$$m \geq \mathcal{M}. \quad (5)$$

The angular momentum  $J_k$  of the end  $i_k$  is given by

$$J_k = \frac{1}{8} (\omega|_{I_{k+1}} - \omega|_{I_k}). \quad (6)$$

The total angular momentum is defined by

$$J = \sum_{k=0}^{N-1} J_k = \frac{1}{8} (\omega|_{I_N} - \omega|_{I_0}). \quad (7)$$

Note the value of the function  $\omega$  at the axis prescribe the angular momentum of the configuration.

The Euler-Lagrange equations of the functional  $\mathcal{M}$  are given by

$$\Delta\sigma - \frac{e^{-2\sigma} |\partial\omega|^2}{\rho^4} = 0, \quad (8)$$

$$\partial_i \left( \frac{\partial^i \omega}{\eta^2} \right) = 0, \quad (9)$$

In these equations  $\Delta = \partial_i \partial^i$  denotes the flat Laplacian in  $\mathbb{R}^3$ . An important property of the functional (4) is that equations (8)–(9) correspond to the stationary axially symmetric Einstein equations.

We are now in position to formulate the variational approach of the inequality (2). The conjecture is the following:

**Conjecture 1** *For arbitrary functions  $(\sigma, \omega)$  we have*

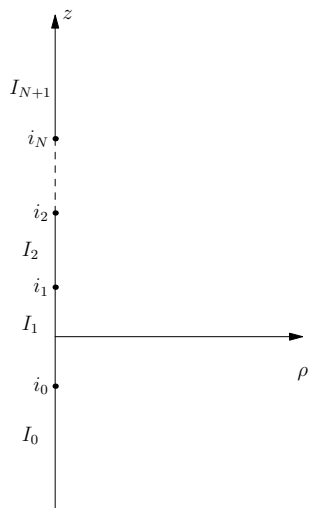
$$\mathcal{M}(\sigma, \omega) \geq \sqrt{|J|}, \quad (10)$$

where  $J$  is given by (7). Moreover, the equality in (10) implies that the functions  $(\sigma, \omega)$  correspond to the extreme Kerr solution. That is, for fixed total angular momentum  $J$ , the extreme Kerr solution is the unique absolute minimum of  $\mathcal{M}$ .

The inequality (2) is a direct consequence of this conjecture and (5). It is important to emphasize that the number of end points  $i_k$  and their corresponding angular momentum  $J_k$  are not fixed. That is, the conjecture states that for fixed  $J$ , extreme Kerr is the unique absolute minimum among all possible Kerr functions  $(\sigma, \omega)$  and among all possible configurations of ends  $i_k$  with individual angular momentum  $J_k$ . Note that in order to have a non zero  $J$  we need at least one end point.

This is a singular variational problem since a non zero  $J$  implies (by equation (7)) that at least one  $J_k$  is non zero, then equation (6) implies that  $\omega$  is discontinuous at  $i_k$  and hence has infinity gradient at this point. In order to make the second term in the integral (4) finite the function  $\sigma$  should diverge at  $i_k$  to compensate the divergence of the gradient of  $\omega$ . Also, the singularity of  $\sigma$  at  $i_k$  can not be too severe because the first term in the integral (4) should remain bounded.

In the formulation of the conjecture we did not specify the functional space of admissible functions  $(\sigma, \omega)$  for the variational problem. As we mentioned above, the functions are typically singular at  $i_k$ , and hence the prescription of the appropriate functional space can be quite subtle. We will no discuss this issue here since it is beyond the scope of this article. For our present purpose, it is enough to assume some space of admissible functions

FIG. 1:  $N$  asymptotic ends

which is regular enough in order that the integral (4) is well defined but it is also compatible with the singular boundary conditions (7) (for a discussion regarding this point see [9])

Conjecture 1 was proved for the case  $N = 1$  in [9] and [10]. The case  $N \geq 2$  is open. Remarkably, for general  $N$  in [10] it has been proved that if the ends  $i_k$  and the individual angular momentum  $J_k$  are fixed then there exists a unique minimum of the functional  $\mathcal{M}$ . This minimum satisfies the Euler-Lagrange equations (8)–(9). That is, for fixed  $i_k$  and  $J_k$ , there exists functions  $(\sigma_{min}, \omega_{min})$ , solutions of (8)–(9), where  $\omega_{min}$  satisfies (6), such that

$$\mathcal{M}(\sigma, \omega) \geq \mathcal{M}_{min}, \quad (11)$$

for all admissible functions  $(\sigma, \omega)$  where  $\omega$  satisfies the boundary condition (6) and we have defined

$$\mathcal{M}_{min} \equiv \mathcal{M}(\sigma_{min}, \omega_{min}). \quad (12)$$

What is not known is the value of  $\mathcal{M}_{min}$ . In particular, it is not known if this minimum satisfies the inequality (10) for  $N \geq 2$ . A natural strategy to prove the conjecture is to prove that for arbitrary  $i_k$  and  $J_k$  the minimum  $\mathcal{M}_{min}$  satisfies (10). The main goal of this article is to compute numerically this value for different configurations, showing that it satisfies the inequality (10) in all considered cases.

In order to compute  $\mathcal{M}_{min}$  we need to calculate the solution  $(\sigma_{min}, \omega_{min})$  of the Euler-Lagrange equations (8)–(9) with boundary conditions (6). As an efficient method for computing numerically both the solution and the value of the energy  $\mathcal{M}$  we propose a heat flow defined as follows. We consider functions  $(\sigma, \omega)$  which depend on the coordinates  $x^i$  and an extra parameter  $t$ . Then, we

define the following flow

$$\dot{\sigma} = \Delta\sigma + \frac{e^{-2\sigma}|\partial\omega|^2}{\rho^4}, \quad (13)$$

$$\dot{\omega} = \eta^2 \partial_i \left( \frac{\partial^i \omega}{\eta^2} \right), \quad (14)$$

where a dot denotes partial derivative with respect to  $t$ . That is, we have added time derivatives to the right hand side of equations (8)–(9). Equations (13)–(14) represent the gradient flow of the energy (4). As  $t \rightarrow \infty$  we expect that the solution of the flow will reach a stationary regime (i.e.  $\dot{\sigma} = \dot{\omega} = 0$ ) and hence it will provide a solution of equations (8)–(9).

The important property of the flow is that the energy  $\mathcal{M}$  is monotonic under appropriate boundary conditions. This can be seen as follows. Consider the functional (4) defined on a bounded domain  $\Omega$  (denoted in the following by  $\mathcal{M}_\Omega$ ) for functions that are solutions of (13)–(14) and take a time derivative of  $\mathcal{M}_\Omega$ . Integrating by parts and using the evolution equations (13)–(14) we obtain

$$\dot{\mathcal{M}}_\Omega = -\frac{1}{16\pi} \int_\Omega (\dot{\sigma}^2 + \eta^{-2} \dot{\omega}^2) d\mu + \frac{1}{16\pi} \oint_{\partial\Omega} (\dot{\sigma} \partial_n \sigma + \eta^{-2} \dot{\omega} \partial_n \omega) ds, \quad (15)$$

where  $ds$  is the area element of the boundary  $\partial\Omega$  and  $\partial_n$  denotes exterior normal derivative with respect to  $\partial\Omega$ . By combining of homogeneous Neumann boundary conditions

$$\partial_n \sigma = 0, \quad \partial_n \omega = 0 \text{ on } \partial\Omega, \quad (16)$$

or Dirichlet boundary conditions

$$\sigma = g_1, \quad \omega = g_2 \text{ on } \partial\Omega, \quad (17)$$

for arbitrary time independent functions  $g_1, g_2$  (since in this case we get  $\dot{\sigma} = \dot{\omega} = 0$  on the boundary) will make the boundary term in (15) vanish. And hence we get that

$$\dot{\mathcal{M}}_\Omega = -\frac{1}{16\pi} \int_\Omega (\dot{\sigma}^2 + \eta^{-2} \dot{\omega}^2) d\mu \leq 0. \quad (18)$$

When the domain  $\Omega$  is  $\mathbb{R}^3$  we need to prescribe appropriate fall off conditions in order to cancel the boundary term in (15). However, as we will discuss in the next section, in the numerical calculations the domain  $\Omega$  is always bounded and hence the boundary conditions (16) and (17) will be used.

The procedure to compute the value of  $\mathcal{M}_{min}$  will be the following. We begin with some arbitrary initial data  $(\sigma, \omega)$  at  $t = 0$  that satisfies the boundary condition (6) for some fixed configuration of  $i_k$  and  $J_k$ . Then we solve numerically the flow equations (13)–(14). The mass  $\mathcal{M}(t)$  will decrease with time, and it will reach the minimum value as  $t \rightarrow \infty$ . This minimum will be of course

independent of the initial data. That is, we expect the following behavior of the solution of the flow equations

$$\lim_{t \rightarrow \infty} \sigma(t) = \sigma_{min}, \quad \lim_{t \rightarrow \infty} \omega(t) = \omega_{min}, \quad (19)$$

and

$$\lim_{t \rightarrow \infty} \mathcal{M}(t) = \mathcal{M}_{min}. \quad (20)$$

Note that (18) implies

$$\mathcal{M}(t) \geq \mathcal{M}_{min} \quad \forall t. \quad (21)$$

The monotonicity property (18), together with the upper bound (21), make the flow equations ideally suited for a numerical study of the inequality (10).

Equations (8)–(9) are essentially harmonic maps with singular boundary conditions. The first existence result for harmonic maps (in compact manifolds without boundaries) used a heat flow [22]. In that reference the behavior (19) was in fact proved. There exists also extensions of this result to include regular boundary conditions [23]. These works were the motivation for the flow equations (13)–(14). We emphasize however, that the existence results presented in [9] [10] for equations (8)–(14) with the singular boundary conditions (6) (which are based on [24]) do not use a heat flow, they use a direct variational method. The numerical calculations presented in this article confirm (19) and hence suggest that a similar existence result can be proved using the present heat flow.

There is some freedom to construct a heat flow out of equations (8)–(9) in such a way that  $\mathcal{M}$  is monotonic under the evolution. Namely we can multiply by arbitrary positive functions the left hand side of (13)–(14) and we still have that  $\dot{\mathcal{M}}$  is negative. The choice made in (13)–(14) appears to be the simplest one because the principal part of the equations are given by heat equations. In effect, we can write equations (13)–(14) as follows

$$\dot{\sigma} = \Delta\sigma + \frac{e^{-2\sigma} |\partial\omega|^2}{\rho^4}, \quad (22)$$

$$\dot{\omega} = \Delta\omega - 4 \frac{\partial_i \omega \partial^i \rho}{\rho} - 2 \partial_i \omega \partial^i \sigma. \quad (23)$$

We also note that in equation (13) we can apply the maximum principle for parabolic equations (see, for example, [25]) to conclude that  $\sigma$  will be positive for all  $t$  if the initial data and boundary conditions are positive.

In this article, the flow (13)–(23) is used as an auxiliary method for computing a solution of the Einstein stationary equations. It is however interesting to point out the relation of this flow with Einstein evolution equations. As we mention above, in axially symmetry Einstein equations reduce, in an appropriate gauge, to a system of wave equations for  $(\sigma, \omega)$ . More precisely, these equations have the structure of “waves maps” (see, for example, [26] for the definition of wave maps). The initial conditions for these equations are essentially the value of  $(\sigma, \omega)$  and the

value of the time derivative  $(\sigma', \omega')$  on a Cauchy surface. For a typical collapse initial data, the system will radiate gravitational waves and reach a final stationary black hole of mass  $m_0$ . The initial energy of the system is given by the total mass  $m$  and it is conserved along the evolution (see [19] for a discussion on this issue). The total angular momentum  $J$  is also conserved along the evolution. We always have  $m_0 \leq m$ . These data can be also evolved using the heat flow. In this case the data are only the value of  $(\sigma, \omega)$  at some time. The total energy of the system is given by  $\mathcal{M}$ , and we have seen that  $m \geq \mathcal{M}$  with equality for momentary stationary data. The system will dissipate energy and reach a final stationary regime with final energy  $\mathcal{M}_{min}$ . We have that  $\mathcal{M}_{min} \leq \mathcal{M}$ . For the two cases, the system will reach a solution of the Einstein stationary equations at late time. These solutions are different, and there is a priori no obvious relation between them. In particular, there is no obvious relation between  $m_0$  and  $\mathcal{M}_{min}$ .

The analogy presented above corresponds essentially to the relation between wave maps, heat flows and harmonic maps which represents a geometric generalization of the relation between wave equation, heat equation and Laplace equation. For the case without symmetries it is not possible to reduce Einstein equation to a wave map but the analogy can still be made if we use the Ricci flow instead of the heat flow. Note however, that in our case the parabolic equations, although non-linear, are much simpler than the Ricci flow equations. For a further discussion about this analogy see [26].

The flow equations will provide a numeric solution  $(\sigma, \omega)$  of equations (8)–(9). As we will see below, the functions  $(\sigma, \omega)$  determine the complete metric of an stationary axially symmetric spacetime. However, although the solution  $(\sigma, \omega)$  is always regular outside the ends  $i_k$ , it turns out that the other components of the metric are, in general, not regular at the axis. That is, not all solutions  $(\sigma, \omega)$  will produce a regular spacetime metric. In particular, it is expected that a solution  $(\sigma, \omega)$  that correspond to many black holes (i.e.  $N \geq 2$  in our setting) do not lead to a regular metric. As we mentioned in the introduction, this is a relevant point in the black hole uniqueness theorem. This is precisely what we observe in the numerical computations presented in section IV. We emphasize however that in order to test the inequality (2) we only need to compute the energy  $\mathcal{M}$  which depends only on  $(\sigma, \omega)$  and not on the other components of the spacetime metric. In particular, the energy  $\mathcal{M}$  is not affected by the possible singular behavior at the axis of the other components of the metric.

To reconstruct the spacetime metric from  $(\sigma, \omega)$  we follow [15]. Assume that  $(\sigma, \omega)$  are solutions of equations (8)–(9). Then, we can define, up to constants, the following functions  $\Omega$  and  $\gamma$  by

$$\gamma_{,\rho} = \frac{1}{4} \rho \eta^{-2} (\eta_{,\rho}^2 - \eta_{,z}^2 + \omega_{,\rho}^2 - \omega_{,z}^2), \quad (24)$$

$$\gamma_{,z} = \frac{1}{2} \rho \eta^{-2} (\eta_{,\rho} \eta_{,z} + \omega_{,\rho} \omega_{,z}), \quad (25)$$

and

$$\Omega_{,z} = \rho \frac{\omega_{,\rho}}{\eta^2}, \quad \Omega_{,\rho} = -\rho \frac{\omega_{,z}}{\eta^2}. \quad (26)$$

The spacetime metric, in coordinates  $(t, \rho, z, \phi)$ , is given by

$$g = -V dt^2 + 2W dt d\phi + \eta d\phi^2 + e^{2u}(d\rho^2 + dz^2), \quad (27)$$

where  $\eta$  is given in terms of  $\sigma$  by (3) and the functions  $V$ ,  $W$  and  $u$  are defined by

$$W = \eta\Omega, \quad V = X^{-1}(\rho^2 - W^2), \quad e^{2u} = \frac{e^{2\gamma}}{\eta}. \quad (28)$$

All functions depend only on  $(\rho, z)$ . The two Killing vectors of the metric are given

$$\xi^\mu = \left(\frac{\partial}{\partial t}\right)^\mu, \quad \eta^\mu = \left(\frac{\partial}{\partial \phi}\right)^\mu, \quad (29)$$

and we have

$$V = -\xi^\mu \xi^\nu g_{\mu\nu}, \quad \eta = \eta^\mu \eta^\nu g_{\mu\nu}, \quad W = \eta^\nu \xi^\mu g_{\nu\mu}, \quad (30)$$

where  $\mu, \nu$  are spacetime indexes. We also have that  $\omega$  is the twist potential of  $\eta^\mu$  (see [15]).

The metric (27) will be regular at the axis if the following condition is satisfied

$$\lim_{\rho_0 \rightarrow 0^+} \frac{\sqrt{\eta}}{\int_0^{\rho_0} e^u d\rho} = 1. \quad (31)$$

For arbitrary solutions  $(\sigma, \omega)$  this condition will not be satisfied and hence the metric will not define a regular solutions of Einstein equations. The singularities at the axis of these kind of metrics are interpreted as the forces needed to balance the gravitational attraction and keep the bodies in equilibrium (see [15] for details).

The regularity condition (31) can be conveniently written in term of a function  $q$  defined by [37]

$$q = u - \frac{\sigma}{2}. \quad (32)$$

This function satisfies the following equations

$$q_{,\rho} = \frac{\rho}{4} (\sigma_{,\rho}^2 - \sigma_{,z}^2) + \frac{\rho}{4\eta^2} (\omega_{,\rho}^2 - \omega_{,z}^2) \quad (33)$$

$$q_{,z} = \frac{1}{2}\rho (\sigma_{,\rho}\sigma_{,z} + \eta^{-2}\omega_{,\rho}\omega_{,z}). \quad (34)$$

Condition (31) implies that

$$q|_{\rho=0} = 0. \quad (35)$$

If the regularity condition fails, we can calculate the value of  $q$  at each component of the axis

$$q_k = q|_{I_k}. \quad (36)$$

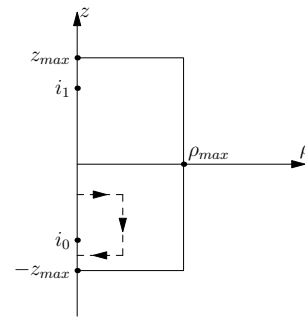


FIG. 2: The bounded domain for the numerical calculation for two black holes located at  $i_0$  and  $i_1$ . The dashed line indicates a typical path for the integration of the function  $q$ .

These values are calculated integrating the gradients (33)–(34) with an appropriate path, see figure 2. The force between the black holes is given by

$$F_k = \frac{1}{4}(e^{-q_k} - 1). \quad (37)$$

Finally, we discuss an important property of the stationary equations (8)–(9), namely their scale invariance (see [27]). Let  $s > 0$  be a real number. Given functions  $\sigma$  and  $\omega$  we define the rescaled functions  $\sigma_s$  and  $\omega_s$  by

$$\sigma_s(\rho, z) = \sigma\left(\frac{\rho}{s}, \frac{z}{s}\right), \quad \omega_s = s^2\omega\left(\frac{\rho}{s}, \frac{z}{s}\right). \quad (38)$$

The functions  $(\sigma_s, \omega_s)$  define solutions of equations (8)–(9) with respect to the rescaled coordinates  $(s\rho, sz)$ . Under this scaling, the physical parameters rescale as

$$J \rightarrow s^2 J, \quad L_k \rightarrow s L_k, \quad (39)$$

and

$$\mathcal{M}(\sigma_s, \omega_s) = s\mathcal{M}(\sigma, \omega). \quad (40)$$

Note that the quotient  $J/L^2$  is scale invariant. In particular, for the case of two black holes, with parameters  $J_1$ ,  $J_0$  and  $L_0$ , the scale invariance of the solution implies that only two parameters are non-trivial.

### III. THE NUMERICAL IMPLEMENTATION

We analyze in this section how to solve numerically the flow equations (13)–(14).

#### A. Equations and boundary conditions

Although the problem has axial symmetry, equations (13)–(14) are written in  $\mathbb{R}^3$  (the Laplace operator corresponds to the flat Laplacian in  $\mathbb{R}^3$ ). We can solve these

equations for arbitrary data, with or without axial symmetry. The minimum will be axially symmetric for any choice of initial data. This is of course possible because the boundary conditions (6) are axially symmetric. The above considerations suggest that we can solve numerically the flow equations in  $\mathbb{R}^3$ . This approach has the advantage that no extra boundary conditions on the axis are needed and also that the equations look more regular in these coordinates. However, from the numerical point of view, this method has two major disadvantages. The first one is that there is a significant loss of resolution because a 3-dimensional grid is used instead of 2-dimensional one. Second, the functions are singular at the end points  $i_k$  and those points are inside the domain. That is, there are grid points at both sides of a singularity and this is very problematic for the finite difference method. We found that it is much more convenient to work in a 2-dimensional grid using cylindrical coordinates and imposing appropriate boundary conditions on the axis, as we describe in the following. The only disadvantage of this approach is that we need to handle terms which are formally singular at the axis. A typical example is the term  $\partial_\rho \sigma / \rho$  which appears in the cylindrical form of the Laplacian in  $\mathbb{R}^3$ , namely

$$\Delta \sigma = \partial_\rho^2 \sigma + \partial_z^2 \sigma + \frac{\partial_\rho \sigma}{\rho}. \quad (41)$$

However, following [28] [29], this kind of terms can be handled numerically in a very satisfactory manner as we will describe below.

Consider  $\mathbb{R}^2$  with coordinates  $(\rho, z)$ . The domain of interest for our problem is the half plane  $\rho \geq 0$ . The axis  $\rho = 0$  is a boundary of the domain. To simplify the notation and the discussion we will focus on the two black hole problem (i.e. we will have only two end points  $i_0$  and  $i_1$  separated by a distance  $L$ ). We emphasize however that the following discussion trivially extends to the general case.

In order to handle the singular behavior of the functions at the points  $i_k$  located on the axis, we decompose the solution as follows. Let  $(\sigma_0, \omega_0)$  be the extreme Kerr solution (see appendix A) centered at the end  $i_0$  with angular momentum  $J_0$ . And let  $(\sigma_1, \omega_1)$  be the extreme Kerr solution centered at  $i_1$  with angular momentum  $J_1$ . Instead of working with  $(\sigma, \omega)$ , which are singular at  $i_k$ , we will work with  $(\bar{\sigma}, \bar{\omega})$  defined by

$$\sigma = \sigma_0 + \sigma_1 + \bar{\sigma}, \quad \omega = \omega_0 + \omega_1 + \bar{\omega}. \quad (42)$$

The idea is that all the singular behavior of the functions are contained in  $(\sigma_0, \omega_0)$  and  $(\sigma_1, \omega_1)$ . We expect the functions  $(\bar{\sigma}, \bar{\omega})$  to be regular during the evolution.

If we insert the ansatz (42) into the flow equations (13)–(14) and use the fact that each pair  $(\sigma_0, \omega_0)$  and  $(\sigma_1, \omega_1)$  are solutions of the stationary equations (8)–(9),

we obtain the following equations for  $(\bar{\sigma}, \bar{\omega})$

$$\begin{aligned} \dot{\bar{\sigma}} = & \Delta \bar{\sigma} + \frac{e^{-2\sigma_0} |\partial \omega_0|^2}{\rho^4} (e^{-2\sigma_1 - 2\bar{\sigma}} - 1) + \\ & \frac{e^{-2\sigma_1} |\partial \omega_1|^2}{\rho^4} (e^{-2\sigma_0 - 2\bar{\sigma}} - 1) + \frac{e^{-2\sigma_0 - 2\sigma_1 - 2\bar{\sigma}}}{\rho^4} (|\partial \bar{\omega}|^2 + \\ & 2\partial_i \omega_0 \partial^i \bar{\omega} + 2\partial_i \omega_1 \partial^i \bar{\omega} + 2\partial_i \omega_0 \partial^i \omega_1), \end{aligned} \quad (43)$$

and

$$\begin{aligned} \dot{\bar{\omega}} = & \Delta \bar{\omega} - 4 \frac{\partial_i \bar{\omega} \partial^i \rho}{\rho} - 2\partial_i \bar{\omega} \partial^i \bar{\sigma} - 2\partial_i \bar{\omega} \partial^i \sigma_0 - 2\partial_i \bar{\omega} \partial^i \sigma_1 - \\ & 2\partial_i \omega_1 \partial^i \sigma_0 - 2\partial_i \omega_0 \partial^i \sigma_1 - 2\partial_i \omega_0 \partial^i \bar{\sigma} - 2\partial_i \omega_1 \partial^i \bar{\sigma}. \end{aligned} \quad (44)$$

These are the equations that we actually solve.

Let us analyze the boundary conditions for equations (43)–(44). We begin with the axis. The boundary conditions for the function  $\bar{\sigma}$  at the axis are given by the regularity conditions. That is,  $\bar{\sigma}$  should be a regular function in  $\mathbb{R}^3$  and hence it should depend smoothly on  $\rho^2$  (see, for example, [30] [31] for a discussion on regularity conditions at the axis for axially symmetric problems) and then at the axis it must satisfy

$$\partial_\rho \bar{\sigma}|_{\rho=0} = 0. \quad (45)$$

We use equation (45) as Neumann boundary conditions at the axis.

For the function  $\bar{\omega}$  the boundary conditions should be such that they do not change the angular momentum during the evolution. Since the angular momentum is prescribed by the value of  $\omega$  at the axis, the natural choice is that the angular momentum is fixed by the values of  $\omega_0$  and  $\omega_1$  at the axis. Hence the appropriate boundary condition for  $\bar{\omega}$  at the axis is the homogeneous Dirichlet one

$$\bar{\omega}|_{\rho=0} = 0. \quad (46)$$

If we consider the whole half plane  $\rho \geq 0$  as domain, then we need to prescribe fall off conditions for  $\bar{\sigma}$  and  $\bar{\omega}$  at infinity compatible with the asymptotic flatness of the solutions (see [9]). In particular, the solutions and its first derivative should go to zero at infinity.

In our case, since the grid is always finite, we need to consider a bounded domain. The domain will be the rectangle  $|z| \leq z_{max}$  and  $0 \leq \rho \leq \rho_{max}$ , where  $z_{max}$  and  $\rho_{max}$  are arbitrary positive constants (see figure 2). Let us denote by  $C$  the part of the boundary that does not contain the axis  $\rho = 0$ . We need to prescribe boundary conditions on  $C$ . These boundary conditions should have two important properties. First, they should imply that the energy on the domain is monotonic under the evolution. Second, in the limit  $z_{max}, \rho_{max} \rightarrow \infty$  they should be compatible with asymptotic flatness. That is, in this limit we want to recover the complete solution on the half plane.

For  $\bar{\sigma}$  we can in principle chose between (16) or (17). Note however that an homogeneous Neumann boundary

condition for  $\sigma$  translate into an inhomogeneous Neumann boundary condition for  $\bar{\sigma}$  (since they are related by equations (42)). Hence, the simpler choice is the homogeneous Dirichlet condition

$$\bar{\sigma}|_C = 0 \quad (47)$$

With this choice is also simpler to extend the function to the whole half plane as we will see below.

For  $\bar{\omega}$  we can not prescribe Neumann boundary condition on  $C$  since if we do so we can not control the value of  $\bar{\omega}$  at the points  $(0, \pm z_{max})$  where  $C$  touch the axis  $\rho = 0$ . In particular, this will be incompatible with (46). Hence, the only possibility is to prescribe an homogeneous Dirichlet condition

$$\bar{\omega}|_C = 0. \quad (48)$$

That is, our set of boundary condition for the numerical evolution is given by (45), (46), (47) and (48).

The variational problem formulated in section II uses  $\mathbb{R}^3$  as domain, which is equivalent, by the axial symmetry, to the the half plane  $\rho \geq 0$ . The fact that in every numerical computation only a finite domain can be used will of course introduce an error. In general it is not easy to measure this error. However, in our case, the variational characterization of  $\mathcal{M}_{min}$  implies that an upper bound of this quantity is always obtained even using a finite grid. This can be seen as follows. Consider the functions  $(\bar{\sigma}, \bar{\omega})$  obtained in the numerical evolution of the flow equations (43)–(44) in the bounded domain  $\Omega$ . These functions are, in principle, only defined in  $\Omega$ . However, we can extend them to  $\mathbb{R}^3$  imposing that they vanish outside  $\Omega$ . And hence, by (42), we get functions  $(\sigma, \omega)$  defined in  $\mathbb{R}^3$ . Since  $(\bar{\sigma}, \bar{\omega})$  vanish on  $\partial\Omega$  (by the boundary conditions (47)–(48)) this extension will be continuous but of course, in general, it will not be differentiable at the boundary  $\partial\Omega$ . However the extension is weakly differentiable. Moreover the weak derivative is square integrable (see, for example, [32] for the definition of weak derivative and also for the proof of this fact). Hence, for the extended functions  $(\sigma, \omega)$  the integral (4) is well defined in  $\mathbb{R}^3$  and they satisfy the boundary conditions (6). That is, they represent admissible test functions for the variational problem. Since  $\mathcal{M}_{min}$  is a minimum we have

$$\mathcal{M}(\sigma, \omega) \geq \mathcal{M}_{min}, \quad (49)$$

where we emphasize that in this equation  $(\sigma, \omega)$  are the extended functions. Note that in  $\mathbb{R}^3 \setminus \Omega$  we have

$$\sigma = \sigma_0 + \sigma_1, \quad \omega = \omega_0 + \omega_1, \quad (50)$$

and hence we can decompose the integral  $\mathcal{M}(\sigma, \omega)$  as follows

$$\mathcal{M}(\sigma, \omega) = \mathcal{M}_\Omega(\sigma, \omega) + \mathcal{M}_{\mathbb{R}^3 \setminus \Omega}(\sigma_0 + \sigma_1, \omega_0 + \omega_1). \quad (51)$$

The first integral will be the result of the numerical computations using the heat flow. The second integral depend only on the explicit functions  $(\sigma_0, \sigma_1; \omega_0, \omega_1)$ . We computed this integral using Maple 9.5.

## B. Numerical methods

We now describe the way we carry out the numerical computations. We use a finite difference scheme to solve the initial-boundary-value problem (IBVP) given by the equations (43)–(44) and boundary conditions (45)–(48). We also perform numerical integrations on the computed solutions to evaluate both the mass  $\mathcal{M}_\Omega$  and the function  $q_1$  (see eq. (36)) used to evaluate the Force (37).

The IBVP is written in cylindrical coordinates  $(\rho, z)$  on the domain  $0 \leq \rho \leq \rho_{max}$  and  $-z_{max} \leq z \leq z_{max}$ . Given two integers  $N_\rho$  and  $N_z$  we define the step-size in the  $\rho$  and  $z$  direction respectively as  $h_z = 2z_{max}/N_z$  and  $h_\rho = \rho_{max}/N_\rho$ . Our equations have singular coefficients at the points  $i_0$  and  $i_1$  on the  $\rho = 0$  axis. These point will be placed, in all our runs, at positions  $z = h_z k$ ,  $k \in \mathbb{Z}$ . The computational grid is defined so that the gridpoint at the site  $(i, j)$  has coordinates

$$\begin{aligned} \rho_i &= \left(i - \frac{3}{2}\right)h_\rho, & i &= 0, 1, 2, \dots, N_\rho + 2, N_\rho + 3, \\ z_j &= \left(j - \frac{3}{2}\right)h_z, & j &= 0, 1, 2, \dots, N_z + 2, N_z + 3, \end{aligned}$$

in this way the uniform grid is half a step size displaced with respect to the coordinate axes and singular points. One can think that the domain is broken into  $N_\rho \times N_z$  cells being each grid point with  $2 \leq i \leq N_\rho + 1$  and  $2 \leq j \leq N_z + 1$  placed at the center of a cell. The gridpoints with  $i = 0, 1, N_\rho + 2, N_\rho + 3$  and  $2 \leq j \leq N_z + 1$  are gridpoints at the center of “ghost cells” used to impose boundary conditions at the  $\rho = \text{const.}$  parts of the boundary. Analogously, the gridpoints with  $j = 0, 1, N_z + 2, N_z + 3$  and  $2 \leq i \leq N_\rho + 1$  are gridpoints at the center of “ghost cells” used to impose boundary conditions at the  $z = \text{const.}$  parts of the boundary. The four gridpoints at each corner of the grid are not used.

Many of the problems we actually compute are symmetric or antisymmetric with respect to the  $z = 0$  plane. In these cases the symmetry is used explicitly to reduce the grid to half-size and so the computer time needed. The grid covers a domain with  $z \geq 0$  (see figure 3).

In our numerical scheme, the four partial derivatives  $\partial_\rho$ ,  $\partial_z$ ,  $\partial_\rho^2$  and  $\partial_z^2$  of  $\bar{\sigma}$  and  $\bar{\omega}$  are approximated by the standard fourth-order accurate symmetric difference operators [33]

$$D = D_0 \left( I - \frac{h}{6} D_+ D_- \right), \quad (52)$$

$$D^2 = D_+ D_- \left( I - \frac{h^2}{12} D_+ D_- \right). \quad (53)$$

Here  $D_+$  and  $D_-$  denote, as usual, the forward and backward difference operators, i.e., if  $f_i$  is a grid function on a 1-dimensional grid with step size  $h$ , we have  $D_+ f_i = (f_{i+1} - f_i)/h$ , and  $D_- f_i = (f_i - f_{i-1})/h$ . To be more explicit we show the approximations to the derivatives with respect to  $\rho$ . If  $u_{i,j} = u(\rho_i, z_j)$ , i.e.,  $u_{i,j}$  denotes the grid function associated to the smooth function

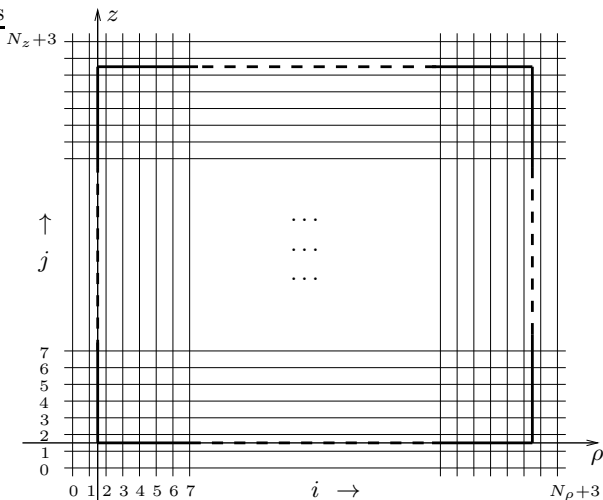


FIG. 3: Computational grid for the symmetric and antisymmetric cases. The gridpoints are at the intersection of the thin lines (cells are not shown). The rectangle in thick lines is the domain for the IBVP.

$u(\rho, z)$ , then

$$\frac{\partial u}{\partial \rho}(\rho_i, z_j) \simeq \frac{\frac{1}{12}u_{i-2,j} - \frac{2}{3}u_{i-1,j} + \frac{2}{3}u_{i+1,j} - \frac{1}{12}u_{i+2,j}}{h_\rho},$$

$$\frac{\partial^2 u}{\partial \rho^2}(\rho_i, z_j) \simeq \frac{-\frac{1}{12}u_{i-2,j} + \frac{4}{3}u_{i-1,j} - \frac{5}{2}u_{i,j} + \frac{4}{3}u_{i+1,j} - \frac{1}{12}u_{i+2,j}}{h_\rho^2}.$$

To carry out the time evolution we use the Du Fort-Frankel method. This method is known to be a good choice for solving parabolic problems because it is explicit and nevertheless unconditionally stable [34] at least when applied for solving an initial value problem. In the notation of [34] (or [33, Sect. 7.3]) we set  $\gamma = 2$ . The  $\gamma$  parameter in this case has to be chosen bigger than  $4/3$  for the method to be stable. The time step can not be chosen big though, and the reason is twofold. First a big time step gives rise to an increasing parasitic solution [33] and more important, the boundary conditions also impose stability restrictions. In the way we treat the boundary conditions (explained below) we have a scheme that is stable as can be seen explicitly in our runs, but this scheme is probably not unconditionally stable. Experimentally we did some runs with a big time step and could see how the solution diverges in few time steps starting at the boundaries (around the singular points  $i_0$  and  $i_1$ ). In most of our computations we use  $h_\rho = h_z = 10^{-2}$  and a time-step  $\delta t = 10^{-4}$ , i.e. the square of the space step-size which is the normal ratio in explicit schemes for parabolic problems. This time step is however, as the equations have singular coefficients, around ten times bigger than the time step we could use with other explicit schemes like 3rd order Runge-Kutta. The Du Fort-Frankel scheme is

only second order accurate but this poses no inconvenience since we are looking for the stationary solution of the parabolic problem. In this case, the truncation error due to the time discretization vanishes when the solution approaches the time independent state.

All the boundary conditions we use are either homogeneous Dirichlet or homogeneous Neumann boundary conditions. The boundary conditions are imposed to a grid function via the points at the ghost cells (see for example [35]). We show, as example, how this is done for boundary conditions (45) and (46). Given the values of  $\bar{\sigma}_{i,j}$  and  $\bar{\omega}_{i,j}$  in the interior of the domain, i.e., for  $2 \leq i \leq N_\rho + 1$  and  $2 \leq j \leq N_z + 1$ , the values at the ghost cells with  $i = 0, 1$  are defined as

$$\begin{aligned} \bar{\sigma}_{0,j} &= \bar{\sigma}_{3,j}, & \bar{\sigma}_{1,j} &= \bar{\sigma}_{2,j}, & (\text{Neumann}), \\ \bar{\omega}_{0,j} &= -\bar{\omega}_{3,j}, & \bar{\omega}_{1,j} &= -\bar{\omega}_{2,j} & (\text{Dirichlet}). \end{aligned}$$

In this way the boundary conditions (45) and (46) are satisfied exactly to the accuracy order of our computations and the same difference operators can be used at all gridpoints inside the domain. As we are using the fourth order accurate operators defined in (52), (53), which have a span of  $\pm 2$  gridpoints, we need two lines of ghost cells outside the domain for each part of the boundary.

We start the time evolution with with initial data that satisfies the right boundary conditions. Now, given the solution at time  $t$  satisfying the right boundary conditions the right hand side of the equations can be computed in the interior of the domain and the time evolution algorithm computes the values of  $\bar{\sigma}$  and  $\bar{\omega}$ , in the interior of the domain, at the next time  $t + \delta t$ . Then the solution at this time is extended to the ghost cells so that it obeys the right boundary conditions and the process is iterated.

Different criteria can be used to stop the time evolution when one is looking for the stationary state. As the main quantity we want to compute in each run is the mass  $\mathcal{M}_\Omega$  of the final stationary solution, we stop the run when the derivative of  $\mathcal{M}_\Omega$  with respect to time becomes, in absolute value, smaller than a given small value.

To compute the mass  $\mathcal{M}_\Omega$  and the value of  $q_1$  we need to approximate two-dimensional and one-dimensional integrals. As the gridpoints are placed at the center of cells that cover the domain of our IBVP, the simplest appropriate rule to approximate these integrals is the midpoint rule. The integrand in (4), when written in cylindrical coordinates, have singular points at  $i_0$  and  $i_1$ . However the midpoint rule provides good enough results. For example, as in our runs we used vanishing initial data, i.e.,  $\bar{\sigma}(t=0) = \bar{\omega}(t=0) = 0$ , the integral in (4) becomes an integral of known, given functions. Thus, we could compare the value obtained with our code to the value obtained with a very precise integration rule—implemented in Maple; in the worst case the relative difference between these values was smaller than  $10^{-3}$ .

### C. Runs and tests

All the solutions of the IBVP we computed can be divided into three groups. The first group consists of symmetric configurations in which  $J_0 = -1.0$  is placed at  $z = -L/2$  and  $J_1 = J_0$  placed at  $z = L/2$ . Within this group we carried out runs for different values of  $L$ , and for different domain sizes. It is clear in this case the solutions  $\sigma$  and  $\omega$  of (13)–(14) are, respectively, symmetric and antisymmetric as functions of  $z$ . Moreover  $\bar{\sigma}$  and  $\bar{\omega}$  satisfy the same symmetry during the whole time evolution of our IBVP—even on a finite domain—provided the domain itself and the initial data are symmetric. The obvious initial data satisfying all boundary conditions and symmetry is  $\bar{\sigma}(t=0) = \bar{\omega}(t=0) = 0$ ; this is what we used in all our runs.

The second group of solutions we computed correspond to antisymmetric configurations in which we placed  $J_0 = -1.0$  at  $z = -L/2$  and  $J_1 = -J_0$  at  $z = L/2$ . We carried out runs for different values of  $L$ . The solutions in this group also have a clear symmetry. In this case both  $\bar{\sigma}$  and  $\bar{\omega}$  are symmetric as functions of  $z$ .

The third group of solutions we computed correspond to asymmetric configurations in which we placed  $J_0 = 1.0$  at  $z = -1/2$  and  $J_1 \neq J_0$  at  $z = 1/2$ . Within this group we carried out runs for various values of  $J_1$ .

When computing solutions in the symmetric or antisymmetric configurations we need to compute the solution in half the domain only,  $z \in [0, z_{max}]$  and  $\rho \in [0, \rho_{max}]$ .  $z = 0$  becomes a boundary and all we need is to use extra boundary conditions at  $z = 0$  that obey the symmetry of the solutions. This boundary conditions are homogeneous Neumann for  $\bar{\sigma}$  and homogeneous Dirichlet for  $\bar{\omega}$  in the symmetric case, and homogeneous Neumann for both functions in the antisymmetric case. By using the symmetry of the solution we reduce to one half the computer time needed.

A main issue, from the point of view of the numerical calculations, is to determine the size of the domain where to compute  $\mathcal{M}_\Omega$ . At the same time we need to estimate error we commit in the determination of  $\mathcal{M}$ . We attack these questions mainly by studying the symmetric case.

The time evolution of  $\mathcal{M}_\Omega$ , for different values of  $L$ , can be seen in figure 4. The initial data in all the runs was set to zero. The smaller the value of  $L$  is the bigger the initial  $\mathcal{M}_\Omega$  is, and also the stronger the equations dissipate so that the code runs for a longer time and the final “stationary”  $\mathcal{M}_\Omega$  turns out to be smaller.

With the purpose of evaluating the precision of the values of mass obtained and of determining a convenient domain size to carry out our computations we performed runs with the same physical parameters but on different domains (and corresponding grids). The results are shown in table I for the two smallest values of  $L$ . In table I “ $\mathcal{M}_{\Omega 0}$ ” is the value of  $\mathcal{M}_\Omega(t=0)$  for vanishing initial data ( $\bar{\sigma}(t=0) = \bar{\omega}(t=0) = 0$ ) as computed by our program; “ $\mathcal{M}_{\Omega 0}^M$ ” is the same quantity as computed by an integration routine of Maple 9.5. “ $\mathcal{M}_\Omega$ ” is the

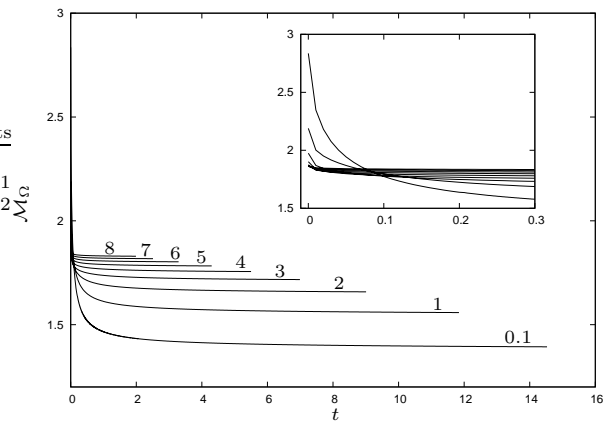


FIG. 4: Time evolution of  $\mathcal{M}_\Omega$  for different values of  $L$  (number close to each curve). In this plot, all the runs were stopped when  $|d\mathcal{M}_\Omega/dt| < 5.0 \times 10^{-4}$ . The detail shows the evolution for a short while  $t \in [0, 0.3]$ .

value computed by our program when the solution is close enough to the stationary state ( $|d\mathcal{M}_\Omega/dt| < 5.0 \times 10^{-4}$  for these runs). “ $\mathcal{M}_0$ ” is the value of the total initial energy, computed with Maple 9.5, on a huge domain  $(\rho, z) \in [0, 40000] \times [-20000, 20000]$ . Finally “ $\mathcal{M}$ ” is given by  $\mathcal{M} = \mathcal{M}_\Omega + (\mathcal{M}_0 - \mathcal{M}_{\Omega 0}^M)$ . On the one hand we have the error introduced by the integration routine. Comparing the second and third columns of the table we see that our integration routine can guarantee three correct figures (two after the decimal point) at initial time. We assume this also holds at final time. On the other hand there is the error introduced by the compactness of the computational domain. Each domain used quadruples the previous domain in size. The values of  $\mathcal{M}$  obtained for the three largest domains are coincident when we round the figures to four digits. Based on this facts we are confident enough as to choose the domain  $(\rho, z) \in [0, 40] \times [-20, 20]$ , in which our code runs fast enough, for all our computations. Hence, we accept as correct the computed values of  $\mathcal{M}$  rounded to three digits. The same domain was used to perform the runs in the antisymmetric and asymmetric cases.

## IV. RESULTS

In this section we present the results of the numerical simulations. As we pointed out above, we will concentrate on the two black holes case with individual momentum  $J_0, J_1$  and separated by a distance  $L$ .

### A. Expected behavior

Let us first discuss, in an heuristic way, the expected behavior of the total mass  $\mathcal{M}_{min}$  of the stationary solution corresponding to this configuration in some asymp-

Domain $(\rho, z)$	$\mathcal{M}_{\Omega_0}$	$\mathcal{M}_{\Omega_0}^M$	Rel. error	$\mathcal{M}_{\Omega}$	$\mathcal{M}_0$	$\mathcal{M}$
$[0, 10] \times [-5, 5]$	2.650041128	2.651146040	$-4.17 \times 10^{-4}$	1.220646770	2.898066024	1.467566754
$[0, 20] \times [-10, 10]$	2.773619709	2.774724666	$-3.98 \times 10^{-4}$	1.332235504	2.898066024	1.455576862
$[0, 40] \times [-20, 20]$	2.835391328	2.836496292	$-3.90 \times 10^{-4}$	1.393365251	2.898066024	1.454934983
$[0, 80] \times [-40, 40]$	2.866221110	2.867326074	$-3.85 \times 10^{-4}$	1.424331374	2.898066024	1.455071324
$[0, 10] \times [-5, 5]$	2.002782916	2.003994940	$-6.05 \times 10^{-4}$	1.381272815	2.251736983	1.629014858
$[0, 20] \times [-10, 10]$	2.127077532	2.128289601	$-5.70 \times 10^{-4}$	1.496600061	2.251736983	1.620047443
$[0, 40] \times [-20, 20]$	2.188941879	2.190153954	$-5.53 \times 10^{-4}$	1.558251402	2.251736983	1.619834431
$[0, 80] \times [-40, 40]$	2.219783296	2.220995372	$-5.46 \times 10^{-4}$	1.589210683	2.251736983	1.619952294

TABLE I: Several runs with the symmetric configuration and the same physical parameters,  $J_0 = J_1 = 1.0$ , but on different domains. In all cases  $h_\rho = h_z = 10^{-2}$ ,  $\delta t = 10^{-4}$  and the initial data was set to zero. The upper half of the table corresponds to  $L = 0.1$  and the lower part to  $L = 1.0$

otic limits.

Consider the far limit  $L \rightarrow \infty$ . In this limit, we expect the interaction between the black holes to be small. If we make an expansion in powers of  $L^{-1}$  of the total mass  $\mathcal{M}_{min}$  the first non-trivial terms should correspond to the sum of the individual masses. The second term should correspond to the Newtonian gravitational interaction energy between the black holes. And finally, the third term should be given by the interaction between the angular momentum of the black holes. This term is called spin-spin interaction in the literature (see [36] [21] for a detailed discussion of this issue). That is, we expect the following expansion

$$\mathcal{M}_{min} \approx m_0 + m_1 - \frac{m_0 m_1}{L} + \frac{2J_0 J_1}{L^3} + O(L^{-4}), \quad (54)$$

where  $m_0 = \sqrt{|J_0|}$  and  $m_1 = \sqrt{|J_1|}$ . This kind of expansion is valid without the assumption of axial symmetry, in fact the formula (54) arises as particular case of the general expansion presented in [36] [21]. Also, for the solution  $(\sigma_{min}, \omega_{min})$  we expect the following behavior in the limit  $L \rightarrow \infty$

$$\sigma_{min} \approx \sigma_0 + \sigma_1, \quad \omega_{min} \approx \omega_0 + \omega_1. \quad (55)$$

The Newtonian interaction is of course always negative. However the sign of the spin-spin interaction depends on the individual signs of the angular momentum  $J_0$  and  $J_1$ . For the aligned case (i.e. when  $J_0$  and  $J_1$  has the same sign) it is positive and hence has opposite sign as the Newtonian interaction. This is the most interesting case regarding the inequality (2) since it is expected to be the most favorable situation to find a counter example to conjecture 1. This can be seen as follows. In a configuration with aligned angular momentum the total amount of angular momentum  $|J|$  (recall that  $J = J_0 + J_1$ ) is always greater than in the anti aligned case. On the other hand the first terms in the expansion (54) are the same in both cases. That is, up to order  $L^{-2}$  we have the same mass in both configurations but the aligned one has greater total angular momentum. Also, from the point of view of the black hole equilibrium problem the aligned configuration is the most interesting one since in this case it is in

principle conceivable that the spin-spin force balance the Newtonian gravitational attraction to make the equilibrium possible at some particular separation distance  $L$ . On the other hand, for the anti aligned case it has been proved that the equilibrium is not possible [17].

Let us discuss now the limit  $L \rightarrow 0$ . In this limit we have only one asymptotic end and hence we expect that the solution approach to a single extreme Kerr solution with angular momentum  $J$ . Let us denote this solution by  $(\sigma_{01}, \omega_{01})$ . This behavior can be justified as follows. Consider the behavior of the individual extreme Kerr solutions  $(\sigma_0, \omega_0)$  and  $(\sigma_1, \omega_1)$ . The sum  $(\sigma_0 + \sigma_1, \omega_0 + \omega_1)$  it is of course not a solution of the stationary equations (8)–(9) even in this limit since the equations are not linear. However, the extreme Kerr solutions have a ‘linear piece’ namely the functions  $\hat{\omega}_0$  and  $\hat{\omega}_1$  which fix the angular momentum of the solution (see equation (A3)). In the limit  $L \rightarrow 0$  this sum corresponds to  $\hat{\omega}_{01}$ . Since this is the part of  $\omega$  that fixes the angular momentum and the solution is unique for fixed angular momentum, the flow equation should produce functions  $(\bar{\sigma}, \bar{\omega})$  such that the final  $(\sigma, \omega)$  approach to the Kerr extreme solution with angular momentum  $J$ . That is, in the limit  $L \rightarrow 0$  we expect the following behavior

$$\mathcal{M} \approx \sqrt{|J|}, \quad (56)$$

and

$$\sigma_{min} \approx \sigma_{01}, \quad \omega_{min} \approx \omega_{01}. \quad (57)$$

In this limit the function  $\bar{\sigma}$  is singular. This can be seen as follows. In the limit  $L \rightarrow 0$ , by equation (A6), the singular behavior of the sum  $\sigma_0 + \sigma_1$  is given by

$$\sigma_0 + \sigma_1 = -4 \log r + O(1). \quad (58)$$

On the other hand, by the same equation (A6), the behavior of the extreme Kerr solution  $\sigma_{01}$  is given by

$$\sigma_{01} = -2 \log r + O(1). \quad (59)$$

Then, in order to reach (59), the function  $\bar{\sigma}$  generated by the flow should be singular in the limit  $L \rightarrow 0$ . This is

$L$	$\mathcal{M}_\Omega$ initial	$\mathcal{M}_\Omega$ final	$\mathcal{M}$
0.1	2.84	1.39	1.45
1.0	2.19	1.56	1.62
2.0	1.98	1.66	1.72
3.0	1.90	1.72	1.78
4.0	1.88	1.76	1.82
5.0	1.87	1.78	1.84
6.0	1.87	1.80	1.86
7.0	1.87	1.82	1.88
8.0	1.87	1.83	1.89

TABLE II: Computed values of  $\mathcal{M}_\Omega$  and final energy  $\mathcal{M}$  for different values of  $L$  in the symmetric configuration. The individual angular momentum parameters are  $J_0 = J_1 = 1$ , and hence we have  $\sqrt{|J|} = \sqrt{2}$ . The domain used was defined by  $z_{max} = 20$  and  $\rho_{max} = 40$ . The grid used (for the semi-domain) is  $4000 \times 2000$  points.

precisely what we observe in our computation as we will see.

Finally, let us discuss the general shape of the curve  $\mathcal{M}_{min}(L)$ . This curve should not have minimum or maximum, since, roughly speaking, a minimum or maximum will signal an equilibrium point. Using the asymptotic limits (54) and (56), we conclude that the curve  $\mathcal{M}_{min}(L)$  should lie between the lines  $\sqrt{|J|}$  and  $\sqrt{|J_0|} + \sqrt{|J_1|}$  and it should be monotonically increasing with  $L$ , that is

$$\frac{\partial \mathcal{M}_{min}(L)}{\partial L} > 0. \quad (60)$$

## B. Results of computations

Let us consider first the symmetric configuration, that is, two black holes with the same angular momentum  $J_0 = J_1 = J$  separated by a distance  $L$ . As we have discussed in section II, by the scale invariance of the equations, we can normalize to  $J = 1$  without loss of generality.

In figures 5 and 6 we present the plots of  $\bar{\sigma}(\rho, z)$  and  $\bar{\omega}(\rho, z)$  for the symmetric case with  $L = 1$  in the semi-domain as a typical plot of the solutions obtained. A detail of each plot near the ends, where most of the variations of the functions occur, is also shown.

Our main result is shown in table II where we present the computed values of  $\mathcal{M}$  (rounded to three digits). Figure 7 shows the plot  $\mathcal{M}$  as function of  $L$ . Clearly all values of  $\mathcal{M}$  are higher than  $\sqrt{2}$  and conjecture 1 is satisfied. Direct observation of figure 7 shows that  $\mathcal{M}$  is a monotonic function of  $L$  and, at least graphically, seems to obey that  $\mathcal{M} \rightarrow \sqrt{2}$  when  $L \rightarrow 0$ . Moreover, although the values of  $L$  for which we could compute the solution are not big, the plot also shows that the limit  $\mathcal{M} \rightarrow 2$  when  $L \rightarrow \infty$  is plausible.

For every value of  $L$  in table II we also computed the force between the black-holes given by equation (37) and

the value of the derivative  $d\mathcal{M}/dL$ . To compute the force we evaluated the corresponding value of  $q_1$  by following ten different trajectories surrounding the end  $i_1$ . We found that the values of  $q_1$ , for the different trajectories, are not the same as expected. The reason is that  $q_1$  is a much more sensitive measurement of “stationarity” of the solution than  $\mathcal{M}$  is and so we would need a much longer evolution to have a good value of  $q_1$  (see explanation below). All the values of  $q_1$  have the right sign though, and the force between the black holes is always attractive. Thus, we present in table III coarse values of the force. It is important to stress, though, that the sign is correct and the value of the force is decreasing with  $L$  in coincidence with the values of the derivative of  $\mathcal{M}$ . Shown values of  $d\mathcal{M}/dL$  were obtained by computing values of  $\mathcal{M}$  at two extra nearby values of  $L + \delta L$  and approximating the derivative by a symmetric finite difference operator.

Naively, we would expect that the force  $F$  is equal to the derivative  $d\mathcal{M}/dL$ . From our data, we observe that this equality appears only to be true in the limit  $L \rightarrow \infty$ . However, since our values for  $F$  are coarse, this difference could in principle be a consequence of numerical errors.

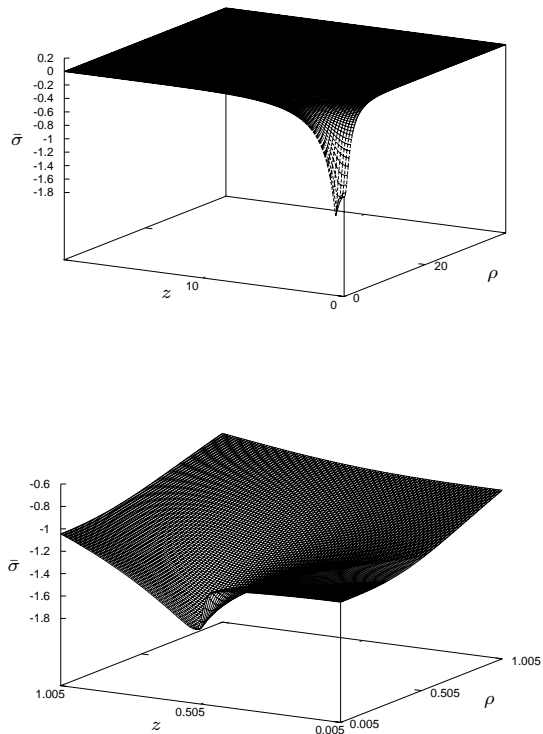


FIG. 5: Plots of  $\bar{\sigma}$  in the semi-domain  $z \in [0, 20]$ ,  $\rho \in [0, 40]$  (above) and detail of the same graph in a small square region  $z \in [0.005, 1.005]$  and  $\rho \in [0.005, 1.005]$  to show the behavior of the solution close to the singular point  $i_1$  (located at  $\rho = 0$  and  $z = 0.05$ ).

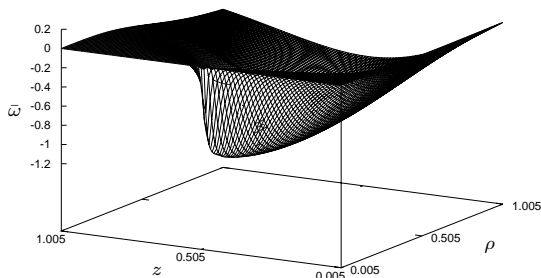
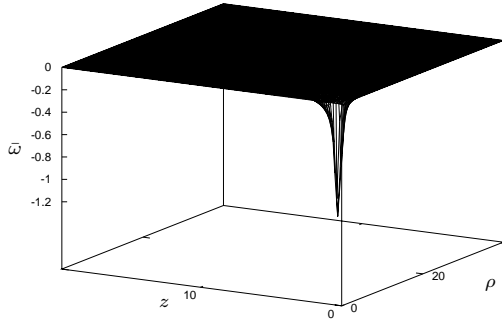


FIG. 6: Plots of  $\bar{\omega}$  in the semi-domain  $z \in [0, 20]$ ,  $\rho \in [0, 40]$  (above) and detail of the same graph in a small square region  $z \in [0.005, 1.005]$  and  $\rho \in [0.005, 1.005]$  to show the behavior of the solution close to the singular point  $i_1$  (located at  $\rho = 0$  and  $z = 0.05$ ).

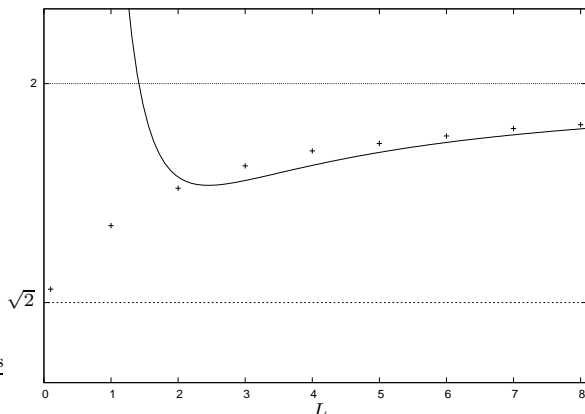


FIG. 7: A plot of the values presented in table II. The individual points are the values of  $\mathcal{M}$ . We have also plotted the Newtonian interaction plus the spin-spin interaction given by equation (54). The two horizontal lines located at 2 and  $\sqrt{2}$  indicate the sum of the individual masses  $m_0 + m_1 = 2$  and the total angular momentum  $J = \sqrt{2}$  respectively.

$L$	$q_1$	$F_1$	$d\mathcal{M}/dL$
0.1	-1.00	0.430	0.247
1.0	-0.53	0.174	0.133
2.0	-0.30	0.088	0.074
3.0	-0.20	0.054	0.047
4.0	-0.14	0.038	0.032
5.0	-0.11	0.028	0.023
6.0	-0.082	0.021	0.017
7.0	-0.067	0.017	0.013
8.0	-0.052	0.013	0.011

TABLE III: Values of  $q_1$ , the attractive force between the black holes and derivative of  $\mathcal{M}$  w.r.t.  $L$ .

Using a small domain, so that our code runs fast, we performed two runs with the same physical parameters ( $L = 1$ ) but stopping the time evolution with two different criteria. The short run stopped when  $d\mathcal{M}/dt < 5.0 \times 10^{-4}$  as most of our runs. The long run stopped when the both the absolute values of the time derivatives of  $\bar{\sigma}$  and  $\bar{\omega}$ , at every site, was smaller than  $10^{-5}$ , i.e., this last criterion sensed stationarity pointwise. When the long run stopped, the value of  $d\mathcal{M}/dt$  was around  $10^{-10}$  but the value of  $\mathcal{M}$  itself was coincident up to four digits to that of the short run. The values of  $q_1$  computed at final time on ten different trajectories around  $i_1$  for both runs showed a variation of 1.27% for the short run and 0.025% for the long run.

The function  $\bar{\sigma}$  is bounded on the whole domain. However, one can see how the peak values of sigma at the symmetry axis,  $\bar{\sigma}(\rho = 0)$ , occur very close or at the singular points  $i_0$  and  $i_1$ . In the symmetric case one, as we have seen in section IV A, we expect that the value of  $\bar{\sigma}$  in the axis, in the region between the ends  $i_0$  and  $i_1$  diverges as  $L \rightarrow 0$ . We could observe this behavior in our numerical solutions. Figure 8 shows the plots of  $\bar{\sigma}(\rho = h_\rho/2, z)$  as function of  $z$ . The expected divergent behavior as  $L \rightarrow 0$  is clearly seen in the graph.

We consider now the anti-symmetric case, where  $J_0 = -J_1$  and separated by a distance  $L$ . Since the total angular momentum in this case is zero, the inequality (10) is trivially satisfied. Nevertheless, it is important to compute this case for testing purpose.

As in the previous case we fixed the angular momentum and normalize them to  $J_0 = 1$  and  $J_1 = -1$ . The results obtained are shown in table IV and plotted in figure 9.

Finally, we consider the asymmetric case, where  $J_0$  and  $J_1$  are separated by a distance  $L = 1$ . We perform runs with  $J_0 = -1$  and varying  $J_1 \in [-1.0, 1.0]$ . This case is interesting because in the limit  $J_1 = 0$  we must recover the one extreme Kerr black hole solution and hence the equality in (10). Note that this limit (as the limit  $L \rightarrow 0$  in the symmetric case) is a singular limit. In both limits we are exploring the neighborhood of the equality in (10) and hence the most favorable cases for a possible counter

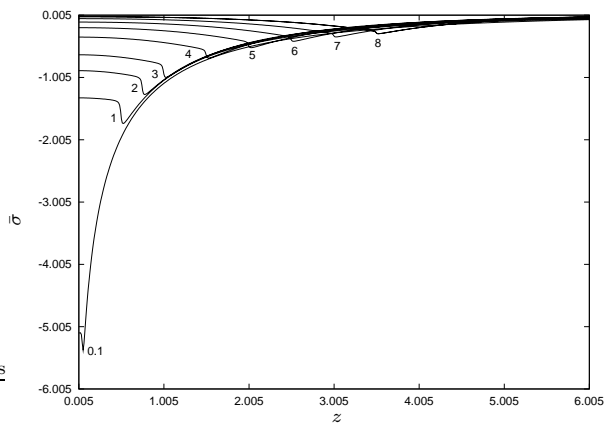


FIG. 8: Plots of  $\bar{\sigma}$  as functions of  $z$  at  $\rho = h_\rho/2$  (the closest gridpoints to the symmetry axis) for different values of  $L$  (numbers close to each curve). Only the  $z > 0$  part of the plot is shown.

$L$	$\mathcal{M}_\Omega$ initial	$\mathcal{M}_\Omega$ final	$\mathcal{M}$
0.5	2.39	1.04	1.10
1.0	2.14	1.35	1.41
2.0	1.95	1.59	1.65
3.0	1.88	1.68	1.75
4.0	1.86	1.74	1.80
5.0	1.86	1.77	1.83
6.0	1.86	1.79	1.86
7.0	1.86	1.81	1.87
8.0	1.86	1.82	1.89

TABLE IV: Computed values of  $\mathcal{M}_\Omega$  and final energy  $\mathcal{M}$  for different values of  $L$  in the antisymmetric configuration  $J_0 = -J_1 = 1$ , where the total angular momentum  $J$  is zero. The domain used was defined by  $z_{max} = 20$  and  $\rho_{max} = 40$ . The grid used (for the semi-domain) is  $4000 \times 2000$  points.

example.

The results are shown in table V and plotted in figure 10. We observe that the inequality (10) is satisfied in all cases.

## V. CONCLUSION

The main result of this article is given in tables II and V. In all cases, we have verified the inequality (10). That is, we have provided strong numerical evidence that this inequality is true for two axially symmetric black holes. Moreover, we have computed a non zero force in the symmetric case (table III) and hence we have also provided numerical evidences that the equilibrium is not possible for two extreme black holes.

The monotonic dependence of the total energy  $\mathcal{M}$  in terms of the separation distance  $L$  plotted in figure 7 suggests a possible strategy to prove analytically the inequality (10). Namely, to study the neighborhood of  $L = 0$  of

the energy. In particular, the first step is to prove that  $d\mathcal{M}/dL > 0$  at  $L = 0$ . Since the value of  $\mathcal{M}$  at  $L = 0$  is known, this will prove the inequality near  $L = 0$ . The second step (probably much more difficult) will be to prove that  $d\mathcal{M}/dL > 0$  for any  $L$ .

Finally, we have also shown that the heat flow equations (13)–(14) constitute an efficient and simple numerical method to construct solutions of the stationary and axially symmetric Einstein equations. We expect that this method can be used also with other kind of boundary conditions.

## Acknowledgments

S. D. thanks Piotr Chruściel for useful discussions. These discussions took place at the Institut Mittag-Leffler, during the program “Geometry, Analysis, and General Relativity”, 2008 fall. S. D. thanks the organizers of this program for the invitation and the hospitality and support of the Institut Mittag-Leffler.

The authors want to thank Luis Lehner and Steve Liebling for useful discussions that took place at FaMAF during their visits in 2008.

S. D. is supported by CONICET (Argentina). This work was supported in part by grant PIP 6354/05 of CONICET (Argentina), grant 05/B415 Secyt-UNC (Argentina) and the Partner Group grant of the Max Planck Institute for Gravitational Physics, Albert-Einstein-Institute (Germany).

## APPENDIX A: EXTREME KERR SOLUTION

The extreme Kerr black hole corresponds to the limit  $m = \sqrt{|J|}$  of the Kerr metric, where  $m$  is the total mass and  $J$  is the angular momentum of the spacetime. Usu-

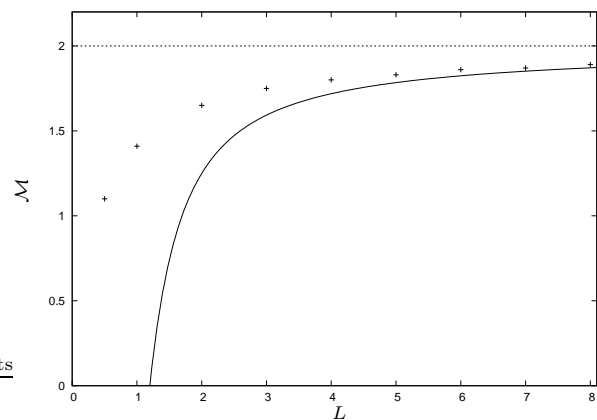


FIG. 9: Total mass in the anti-symmetric case as function of  $L$ .  $J_0 = -1$  is located at  $z = -L/2$  and  $J_1 = 1$  is located at  $z = L/2$ . The semi-domain is  $(\rho, z) \in [0, 40] \times [0, 20]$ . The continuous line is the Newtonian plus spin-spin interaction.

$J_1$	$\mathcal{M}_\Omega$ initial	$\mathcal{M}_\Omega$ final	$\mathcal{M}$	$\sqrt{ J }$
-1.0	2.19	1.56	1.62	1.41
-0.9	2.12	1.52	1.58	1.38
-0.8	2.06	1.49	1.54	1.34
-0.7	1.98	1.45	1.50	1.30
-0.6	1.91	1.41	1.46	1.26
-0.5	1.82	1.36	1.41	1.22
-0.4	1.72	1.32	1.36	1.18
-0.3	1.61	1.27	1.30	1.14
-0.2	1.48	1.21	1.24	1.10
-0.1	1.32	1.13	1.16	1.05
0.0	0.98	0.98	1.00	1
0.1	1.30	1.10	1.13	0.95
0.2	1.46	1.15	1.18	0.89
0.3	1.59	1.18	1.22	0.84
0.4	1.69	1.21	1.25	0.77
0.5	1.78	1.24	1.28	0.71
0.6	1.87	1.24	1.31	0.63
0.7	1.94	1.28	1.34	0.55
0.8	2.02	1.30	1.36	0.45
0.9	2.08	1.33	1.39	0.32
1.0	2.14	1.35	1.41	0

TABLE V: Computed values of  $\mathcal{M}_\Omega$  and final energy  $\mathcal{M}$  in the asymmetric configuration as function of  $J_1$ , where  $J_0 = -1$ . The separation distance is  $L = 1$  and the location of  $i_0$  is fixed at  $z = -0.5$  and  $i_1$  is fixed at  $z = 0.5$ . The domain used was defined by  $z_{max} = 20$  and  $\rho_{max} = 40$ . The grid used is  $4000 \times 4000$  points.

ally, instead of  $J$  in the literature the parameter  $a = J/m$  is used, the extreme limit correspond to  $a = \pm m$ .

Using the notation of section II, for the extreme Kerr black hole we have only one end  $i_0$  located at the origin. The explicit form of the functions  $(\sigma_0, \omega_0)$  are given by

$$\sigma_0 = \log \eta_0 - 2 \log \rho, \quad \omega_0 = \hat{\omega}_0 - \frac{2J^3 \cos \theta \sin^4 \theta}{|J|\Sigma}, \quad (\text{A1})$$

where

$$\eta_0 = \left( \tilde{r}^2 + |J| + \frac{2|J|^{3/2} \tilde{r} \sin^2 \theta}{\Sigma} \right) \sin^2 \theta, \quad (\text{A2})$$

$$\hat{\omega}_0 = 2J(\cos^3 \theta - 3 \cos \theta), \quad (\text{A3})$$

and

$$\tilde{r} = r + \sqrt{|J|}, \quad \Sigma = \tilde{r}^2 + |J| \cos^2 \theta. \quad (\text{A4})$$

In these equations,  $(r, \theta)$  are spherical coordinates in  $\mathbb{R}^3$  related with the cylindrical coordinates  $(\rho, z)$  by the standard formulas  $r = \sqrt{\rho^2 + z^2}$  and  $\tan \theta = \rho/z$ .

In this equations,  $J$  is an arbitrary constant. It gives the angular momentum and it is the only free parameter in this solution. In agreement with equation (6), we have

$$\omega_0(\theta = 0) = -4J, \quad \omega_0(\theta = \pi) = 4J. \quad (\text{A5})$$

Note that the angular momentum is given by  $\hat{\omega}_0$ , the other part of  $\omega_0$  vanishes at the axis.

The singular behavior of  $\sigma_0$  at  $i_0$  is given by

$$\sigma_0 = -2 \log r + O(1). \quad (\text{A6})$$

The sign change  $J \rightarrow -J$  implies  $\sigma \rightarrow \sigma$  and  $\omega \rightarrow -\omega$ . The limit  $J = 0$  correspond to flat spacetime and it is given by

$$\sigma_0 = 0, \quad \eta_0 = \rho^2, \quad \omega_0 = 0. \quad (\text{A7})$$

The important property of the functions  $(\sigma_0, \omega_0)$  is that they are solutions of equations (8)–(9). In the above equations the end point  $i_0$  is chosen to be at the origin of the coordinate system. We have the obvious freedom to translate this point to an arbitrary location. In particular, the extreme Kerr solution centered at the point  $i_1$  used in section III is given by

$$\sigma_1 = \sigma_0(\rho, z - L/2), \quad \omega_1 = \omega_0(\rho, z - L/2). \quad (\text{A8})$$

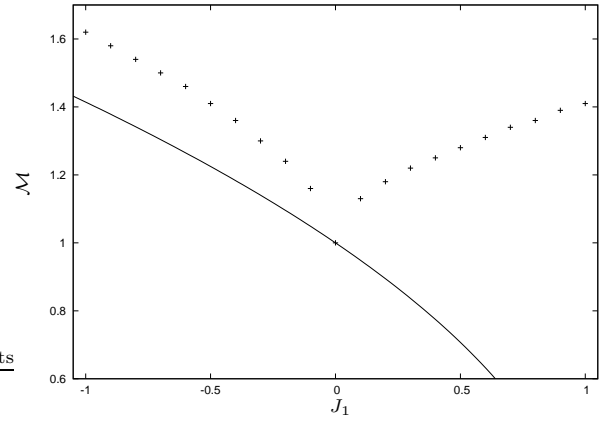


FIG. 10: Total mass in the asymmetric case as function of  $J_1$ .  $J_0 = -1$  is located at  $z = -1/2$  and  $J_1$  is located at  $z = 1/2$ . The semi-domain is  $(\rho, z) \in [0, 40] \times [0, 20]$ . The continuous line is the lower bound according to the conjecture 1

- [1] R. Penrose, Ann. New York Acad. Sci. **224**, 125 (1973).  
[2] R. Wald, in *Black Holes, Gravitational Radiation and the Universe*, edited by B. R. Iyer and B. Bhawal (Kluwer Academic, Dordrecht, 1999), vol. 100 of *Fundamental*

*Theories of Physics*, pp. 69–85, gr-qc/97110068.

- [3] G. Huisken and T. Ilmanen, J. Differential Geometry **59**, 352 (2001).  
[4] H. L. Bray, J. Differential Geometry **59**, 177 (2001),

- math.DG/9911173.
- [5] H. L. Bray and P. T. Chruściel, in *The Einstein equations and the large scale behavior of gravitational fields* (Birkhäuser, Basel, 2004), pp. 39–70.
- [6] S. Dain, Phys. Rev. Lett. **96**, 101101 (2006), ISSN 0031-9007, gr-qc/0511101.
- [7] S. Dain, Class. Quantum Grav. **23**, 6857 (2006), ISSN 0264-9381, gr-qc/0508061.
- [8] S. Dain, Class. Quantum Grav. **23**, 6845 (2006), ISSN 0264-9381, gr-qc/0511087.
- [9] S. Dain, J. Differential Geometry **79**, 33 (2008), gr-qc/0606105.
- [10] P. T. Chruściel, Y. Li, and G. Weinstein, Ann. Phys. **323**, 2591 (2008), arXiv:0712.4064.
- [11] P. T. Chruściel and J. Lopes Costa (2008), 0806.0016.
- [12] G. Weinstein, Comm. Partial Differential Equations **21**, 1389 (1996), ISSN 0360-5302.
- [13] G. Weinstein, Trans. Amer. Math. Soc. **343**, 899 (1994), ISSN 0002-9947.
- [14] G. Weinstein, Comm. Pure App. Math. **45**, 1183 (1992), ISSN 0010-3640.
- [15] G. Weinstein, Comm. Pure App. Math. **43**, 903 (1990), ISSN 0010-3640.
- [16] Y. Y. Li and G. Tian, Commun. Math. Phys. **149**, 1 (1992), ISSN 0010-3616.
- [17] Y. Y. Li and G. Tian, Manuscripta Math. **73**, 83 (1991).
- [18] V. S. Manko and E. Ruiz, Class. Quantum Grav. **18**, L11 (2001), URL <http://stacks.iop.org/0264-9381/18/L11>.
- [19] S. Dain, Class. Quantum Grav. **25**, 145021 (2008), 0804.2679.
- [20] S. Dain, International Journal of Modern Physics D **17**, 519 (2008), arXiv:0707.3118 [gr-qc].
- [21] S. Dain, Phys. Rev. D **66**, 084019 (2002), ISSN 0556-2821, gr-qc/0207090.
- [22] J. Eells, Jr. and J. H. Sampson, Amer. J. Math. **86**, 109 (1964), ISSN 0002-9327.
- [23] R. S. Hamilton, *Harmonic maps of manifolds with boundary* (Springer-Verlag, Berlin, 1975), lecture Notes in Mathematics, Vol. 471.
- [24] G. Weinstein, Math. Res. Lett. **3**, 835 (1996), ISSN 1073-2780.
- [25] L. C. Evans, *Partial differential equations*, vol. 19 of *Graduate Studies in Mathematics* (American Mathematical Society, Providence, RI, 1998), ISBN 0-8218-0772-2.
- [26] T. Tao, *Nonlinear dispersive equations*, vol. 106 of *CBMS Regional Conference Series in Mathematics* (Published for the Conference Board of the Mathematical Sciences, Washington, DC, 2006), ISBN 0-8218-4143-2, local and global analysis.
- [27] D. Sudarsky and R. M. Wald, Phys. Rev. D **47**, R5209 (1993).
- [28] D. Garfinkle and G. C. Duncan, Phys. Rev. **D63**, 044011 (2001), gr-qc/0006073.
- [29] M. W. Choptuik, E. W. Hirschmann, S. L. Liebling, and F. Pretorius, Class. Quant. Grav. **20**, 1857 (2003), gr-qc/0301006.
- [30] O. Rinne (2005), gr-qc/0601064.
- [31] O. Rinne and J. M. Stewart, Class. Quant. Grav. **22**, 1143 (2005), gr-qc/0502037.
- [32] D. Gilbarg and N. S. Trudinger, *Elliptic Partial Differential Equations of Second Order* (Springer-Verlag, Berlin, 2001), ISBN 3-540-41160-7, reprint of the 1998 edition.
- [33] B. Gustafsson, H.-O. Kreiss, and J. Olinger, *Time dependent problems and difference methods*, Pure and Applied Mathematics (John Wiley & Sons Inc., New York, 1995), a Wiley-Interscience Publication.
- [34] D. Gottlieb and B. Gustafsson, SIAM J. Numer. Anal. **13**, 129 (1976), URL <http://www.jstor.org/stable/2156474>.
- [35] O. Rinne, Ph.D. thesis, University of Cambridge (2005).
- [36] R. Wald, Phys. Rev. D **6**, 406 (1972).
- [37] In references [15] [16] a rescaling of this function is denoted by  $\beta$ , we have the relation  $\beta = 2q$